Nanoscale

Accepted Manuscript

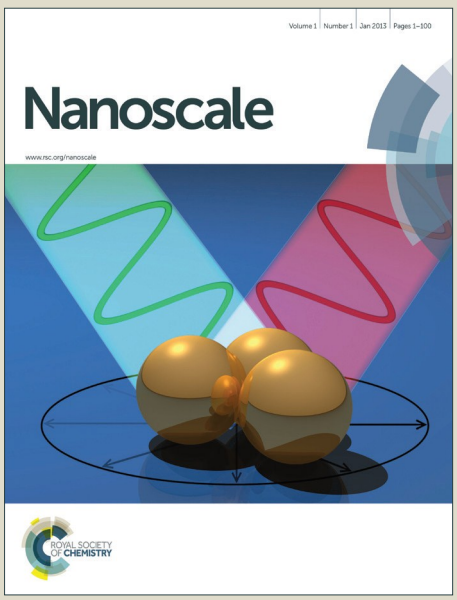

ROYAL SOCIETY OF CHEMISTRY

www.rsc.org/nanoscale

Nanoscale

Cite this: DOI: 10.1039/c0xx00000x

www.rsc.org/xxxxxx

Full Article

Solution-Processed Molybdenum Oxide Treated Silver Nanowire Network: A Highly Conductive Transparent Conducting Electrode with Superior Mechanical and Hole Injection Properties

Jung-Hao Chang,[a] Kai-Ming Chiang,[a] Hao-Wei Kang,[a] Wei-Jung Chi,[a] Jung-Hung Chang,[b] Chih-I Wu[b] and Hao-Wu Lin*[a]

Received (in XXX, XXX) XthXXXXXXXXX 20XX, Accepted Xth XXXXXXXXX 20XX
DOI: 10.1039/b000000x

We demonstrate the fabrication of solution-processed MoO_x-treated (s-MoO_x) silver nanowire (AgNW) transparent conductive electrodes (TCEs) utilizing low-temperature (sub-100 °C) processes. The s-MoO_x can aggregate around the AgNW and formed gauze-like MoO_x thin films between the mesh, which can effectively lower the junction resistance by more than two orders of magnitude. Notably, this s-MoO_x-treated AgNW TCEs exhibit a combination of several promising characteristics, such as high and broad transmittance across a wavelength range of 400 to 1000 nm, transmission of up to 96.8%, low sheet resistance of 29.8 ohm/sq, low haze value of 0.90%, better mechanical properties against bending and adhesion tests, and preferable gap states for efficient hole injection in optoelectronic applications. By utilizing these s-MoO_x-treated AgNW TCEs as the anode in ITO-free organic light emitting diodes, promising performance of 29.2 lm/W and 10.3% external quantum efficiency are demonstrated. The versatile, multi-functional s-MoO_x treatment presented here paves the way for the use of low-temperature, solution-processed MoO_x as both a nanowire linker and a hole injection interfacial layer for future flexible optoelectronic devices.

Introduction

Transparent conducting electrodes (TCEs) play an essential role in a variety of optoelectronic devices, including light-emitting diodes, touch panels, liquid crystal displays, and solar cells. Indium tin oxide (ITO) TCE films are currently dominant in such applications because of their mature fabrication method, relatively high transparency, and low sheet resistance (R_{sheet}). However, high-quality ITO coatings can only be obtained with expensive vacuum processing and high-temperature annealing. The brittle nature of ITO also makes it difficult to use in flexible devices. Several alternative materials, including highly conductive poly(3,4-ethylene dioxythiophene):poly(styrenesulfonate) (PEDOT:PSS),[1-3] carbon nanotubes,[4-6] metal grids,[7] graphene,[8-11] and silver nanowires (AgNWs),[12-22] have been intensively investigated as replacements for ITO.

[a]*Department of Materials Science and Engineering, National Tsing Hua University, No. 101, Section 2, Kuang-Fu Road, Hsinchu 300, Taiwan. E-mail: hwlin@mx.nthu.edu.tw*
[b]*Department of Electrical Engineering and Graduate Institute of Photonics and Optoelectronics, National Taiwan University, Taipei 106, Taiwan.*

Among all the alternatives, AgNWs have demonstrated good optoelectronic characteristics, high mechanical flexibility, and compatibility with low-cost solution processing. These factors make AgNWs the most promising candidate as a next generation TCE. However, there are still issues associated with their utilization in modern optoelectronic devices. These issues include the high R_{sheet} of a dilute pristine AgNW matrix and poor adhesion of this matrix to the substrate.[23] Recently, it has been reported that the R_{sheet} of an AgNW network is dominated by the contact resistance of inter-nanowire junctions.[24, 25] Treatments that have been proposed to reduce junction resistance include high-temperature welding,[23] high-force pressing,[26] ITO nanoparticle fusing,[27] metal oxide particle fusing,[27, 28] plasmonic welding,[29] pulsed light welding[30] and electrical current welding.[20] However, some of these methods involve processes with high energy consumption or treatments of long duration, while others suffer from scalability issues and chemical damage effects.

Recently, efficient hole extraction has been demonstrated with a molybdenum oxide (MoO_x) interfacial layer in organic light-emitting diodes (OLEDs) and organic solar cells.[31-35] MoO_x is a *p*-type semiconductor that selectively conducts holes with an ionization potential of ~ 5.3 eV and an electron affinity of ~ 2.2 eV.[36, 37] However, there is strong evidence in the literature that MoO_x films could in fact be *n*-type semiconductors with significantly deeper energy levels than previously assumed.[38, 39] In addition, while MoO_x with oxygen defects is an intrinsic *n*-type material, reports have shown that MoO_x with gap states, which are measured by ultraviolet photoemission spectroscopy (UPS) and X-ray photoelectron spectroscopy (XPS), can enhance the extraction and injection of both electrons and holes at the interface.[40, 41] Therefore, in this study, we take advantage of this unique property of MoO_x, and prepare it by facile solution processing or vacuum evaporation on an AgNW matrix, in order to lower the inter-nanowire junction resistance and thereby improve the R_{sheet} of an AgNW TCE.

We found that solution-processed MoO_x (s-MoO_x) can aggregate around AgNW junctions and effectively lower the junction resistance and hence R_{sheet} of the film by more than two orders of magnitude. It has been reported that solution-processed TiO_2 can effectively improve the AgNW film conductivity.[28] During solvent evaporation of the TiO_2 solution, the volume of TiO_2 shrinks. The dehydrated TiO_2 aggregation will drive the crossed AgNWs tighter and result in better contact between AgNWs at the junctions. Since the conductivity of MoO_x ($\approx 10^{-11}$

S/cm) is even lower than that of TiO_2 (≈ 10^{-8} S/cm), it is most unlikely that MoO_x aggregation can act as conducting connector between AgNWs.[42, 43] As a result, we believe the enhancement of film conductivity in this work is due to the capillary forces induced closer packing of AgNWs, which is similar to the solution-processed TiO_2 case. By utilizing an optimized concentration of s-MoO_x solution, a TCE is produced that has high average transmittance ($T_{average}$) of 94.8% in the visible to near-infrared wavelength range, maximum transmittance of 96.8% at 565 nm, low R_{sheet} down to 29.8 ohm/sq, and low haze value of 0.90%. This s-MoO_x-treated AgNW network not only shows excellent optical and electrical properties, but also exhibits improved mechanical properties against bending and adhesion tests, and simultaneously provides a preferable energy level for effective hole injection. This last feature is particularly important for active optoelectronic devices such as LEDs, in which the TCE not only acts as a conductor, but also takes the role of the anode that injects holes to the active semiconducting layers.

Experimental

Materials

Silver nanowires suspended in ethanol with a concentration of 10 mg/mL were purchased from *Blue Nano Incorporation* and used as received. The mean length and diameter of the AgNWs were 15 μm and 35 nm, respectively. The s-MoO_x precursor ammonium heptamolybdate ($(NH_4)_6Mo_7O_{24}•4H_2O$) was purchased from *Aldrich* and used as received.

Fabrication of s-MoO_x-treated and vacuum-evaporated MoO_x-treated (e-MoO_x) AgNWs networks

Glass substrates were cleaned in an ultrasonic bath with deionized water, acetone, and then methanol for 15 minutes each. The glass substrates were then UV-ozone treated before AgNW layer deposition. The AgNW dispersion was diluted to 1.42 mg/mL with alcohol and then cast onto the glass substrate by a home-made bar-coating machine with bar speed of 500 mm/s (controlled by a servomotor).[44] The bar-coating process was performed on a hot plate at 50 °C, and the AgNW films remained on the hot plate for ~ 5 minutes to evaporate the residual solvent. The coating process was performed inside a nitrogen-filled glove box. The MoO_x precursor solution was prepared by dissolving ammonium heptamolybdate (160 mg) in deionized water (1 mL) at 80 °C for 1 hour in air. The MoO_x precursor solution was further diluted by deionized water to the desired concentrations (5, 20, 40, 80 and 160 mg/mL). The s-MoO_x was spin-coated from the precursor solution at 4000 rpm for 40 s and annealed at 100 °C for 10 minutes either inside the N_2-filled glove box or in air. The e-MoO_x layer was prepared by thermal evaporation of MoO_x powders in a vacuum chamber with a base pressure of ~ 1 × 10^{-6} Torr. The thickness of the e-MoOx was monitored using a quartz crystal microbalance.

Organic light emitting diode fabrication

Prior to organic thin-film deposition, the TCEs were prepared by the above-mentioned method with the following four conditions: **(A)** pristine AgNW, **(B)** e-MoO_x-treated AgNW (20 nm), **(C)** s-MoO_x-treated AgNW (20mg/mL, annealed in N_2) and **(D)** s-MoO_x-treated AgNW (20 mg/mL, annealed in air). The samples were then transferred to a vacuum chamber with a base pressure of ~ 1 × 10^{-6} Torr for organic material, salt, and metal deposition. For the other layers in the OLEDs, the following materials were used: dipyrazino[2,3-*f*:2′ipyr*h*]quinoxaline-2,3,6,7,10,11-hexacarbonitrile (HAT-CN); *N,N'*-Di(1-naphthyl)-*N,N'*-diphenyl-(1,1')-4,4'-diamine (NPB); 4,4'-Bis(*N*-carbazolyl)-1,1'-biphenyl (CBP); Tris[2-phenylpyridinato-C^2,*N*]iridium(III) ($Ir(ppy)_3$); 3,3'-[5'-[3-(3-Pyridinyl)phenyl][1,1':3',1"-terphenyl]-3,3"-diyl]bispyridine (TmPyPB); CsF; and Al. The device structure was configured as follows: glass / **(A)–(D)** / HAT-CN (10 nm) / NPB:HAT-CN (1.5%, 185 nm) / CBP (5 nm) / CBP:$Ir(ppy)_3$ (8%, 20 nm) / TmPyPB (20 nm) / CsF (1 nm) / Al.

TCE and OLED characteristics measurements

Transmittance, reflectance, and diffuse-transmission spectra of the TCEs were collected using a UV2600 UV-visible spectrophotometer (SHIMADZU) with an integrating sphere. R_{sheet} measurements of the TCEs were taken using the four-point probe method. The nanostructure and surface morphology of the electrodes were imaged using a field emission scanning electron microscope (FE-SEM) (JSM-7000F, JAPAN ELECTRON OPTICS LABORTARY CO., LTD). Atomic force microscopy (AFM) images were analyzed with a Bruker Dimension Icon® Atomic Force Microscope operating in tapping mode. The OLED characteristics were measured by a Keithley 2636A Sourcemeter (Keithley Instruments, Inc.) and a silicon photodetector calibrated by a PR-650 SpectraScan colorimeter (Photo Research, Inc.). The ultraviolet photoemission spectroscopy and X-ray photoelectron spectroscopy were taken in an ultra-high vacuum chamber with a base pressure of 10^{-10} Torr. The UPS valence band spectra were measured with He I (21.2 eV) as the excitation source. XPS measurements were performed using an Al K (1486.6 eV) source. The resolutions of UPS and XPS were 0.15 and 0.5 eV, respectively.[45, 46]

Results and discussion

A schematic diagram of the experimental procedure is shown in **Figure 1**. The AgNW dispersion was diluted to the desired concentration and bar-coated onto the cleaned glass substrate (3 cm × 3 cm) inside an N_2-filled glove box. Subsequently, solutions of MoO_x precursor with varying concentration, ranging from 0 to 160 mg/mL in deionized water, were spin-coated directly onto the pre-deposited AgNW network and annealed at 100 °C in either N_2 atmosphere or air. Upon annealing, the aggregation of MoO_x generated at the AgNW junction and formed a MoO_x-linked AgNW network. The nano-morphology of the resulting s-MoO_x-treated AgNW network was observed by SEM and the images are shown in **Figure 2**. **Figure 2 (a)** displays the pristine AgNW mesh formed by the bar-coating method, where the AgNWs show random orientation and distribution. Owing to capillary action, all the AgNW junctions are linked after s-MoO_x treatment, as shown in **Figure 2 (b) – (e)**. Intriguingly, the lower concentration treatments (**Figure 2 (b) – (d)** and **Figure S1** in supporting information) show gauze-like MoO_x thin films between the mesh. By contrast, the high concentration treatment (**Figure 2 (e)**) exhibits larger pellet-shaped MoO_x precipitates adhering to the AgNWs. For comparison, e-MoO_x was also deposited on the AgNW matrix (see **Figure 2 (f)**). The morphology of this sample is much different from the s-MoO_x-treated AgNW networks, where the e-MoO_x homogeneously covers the AgNWs and the surface topology is the same as the pristine AgNW mesh (**Figure 2 (a)**).

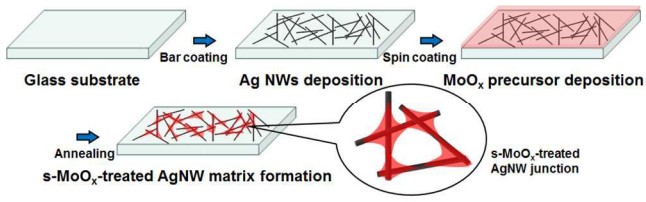

Figure 1. Schematic diagram of the procedure for fabricating s-MoO_x-treated AgNW composite transparent conducting electrodes.

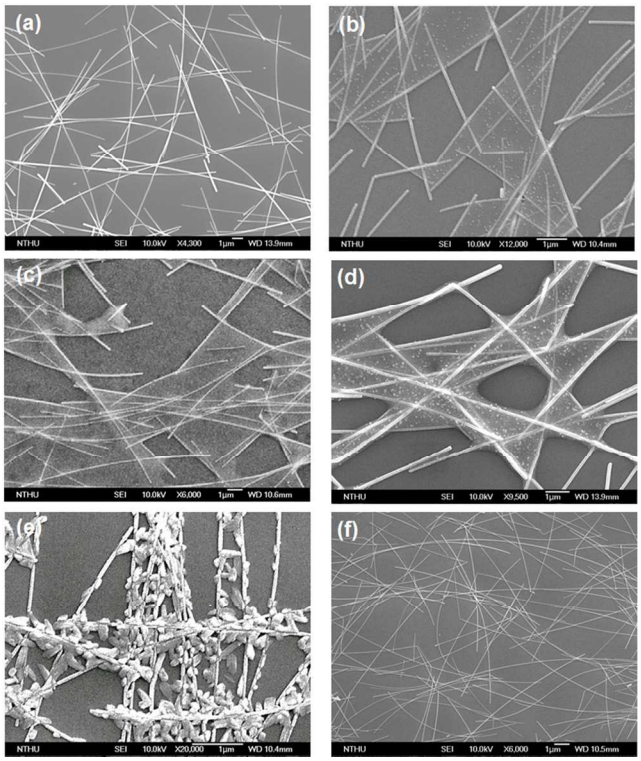

Figure 2. SEM images of (a) pristine AgNWs, (b) s-MoO_x-treated AgNW 5 mg/mL, (c) s-MoO_x-treated AgNW 20 mg/mL, (d) s-MoO_x-treated AgNW 40 mg/mL, (e) s-MoO_x-treated AgNW (160 mg/mL) and (f) e-MoO_x-treated AgNW (30 nm). All s-MoO_x-treated samples shown were annealed in N_2.

The R_{sheet} of s-MoO_x-treated AgNW and e-MoO_x-treated AgNW TCEs are shown in **Figure 3 (a)**. The R_{sheet} dramatically decreases from 4411 ohm/sq to 47.3 ohm/sq with a 5-mg/mL s-MoO_x precursor solution spin-coated and annealed in N_2. The R_{sheet} reaches lowest value of 29.8 ohm/sq using a 20-mg/mL MoO_x precursor solution. This resistance value is over two orders of magnitude lower than that of the pristine AgNW matrix. A similar trend can be observed if the precursor is annealed in air, resulting from the same gauze-like MoO_x between the AgNW mesh as shown in **Figure S2**. However, the samples annealed in N_2 slightly outperform the samples annealed in air, which could be due to the different electronic characteristics of MoO_x prepared in various atmospheres. These characteristics will be discussed further later, when XPS and UPS results are presented. The effect of the e-MoO_x treatment on the AgNW matrix is also shown in the inset of **Figure 3 (a)**. Only a slight decrease in R_{sheet} is observed in e-MoO_x-treated samples, indicating that without solvent evaporation and volume shrinkage processes of s-MoO_x, solely adding MoO_x on AgNWs by thermal evaporation cannot effectively lower the R_{sheet}. The results clearly indicate that s-MoO_x is more suitable than e-MoO_x for conductivity enhancement in AgNW-based TCEs.

To investigate the optical properties of MoO_x-treated AgNW TCEs, a UV-Vis spectrometer with an integrating sphere was used to measure the total transmittance (T), total reflectance (R), and diffuse transmission of the samples. The results are shown in **Figure 4** and the key parameters are summarized in **Table 1**. The total transmittance of the TCE decreases with an increase in the concentration of the s-MoO_x precursor solution and the thickness of the e-MoO_x layer. Compared to the pure AgNW-based TCE without MoO_x treatment ($T_{average}$ = 96.7%, R_{sheet} = 4411 ohm/sq),

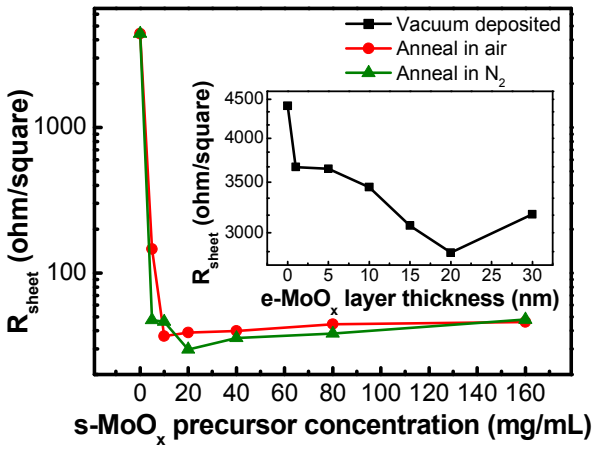

Figure 3. R_{sheet} of the s-MoO_x-treated AgNW matrix annealed in N_2 or air. Inset: R_{sheet} of the e-MoO_x-treated AgNW matrices.

the s-MoO_x-treated AgNW-based TCEs using 5 and 20 mg/cm^3 precursor concentrations only show negligible reductions of $T_{average}$ of 0.5% and 0.8%, respectively, but greatly reduced R_{sheet} values of 47.3 and 29.8 ohm/sq, respectively. The reduction of R_{sheet} by more than two orders of magnitude is attributed to s-MoO_x effectively joining AgNW junctions. Furthermore, because the s-MoO_x only aggregates locally at the inter-nanowire junctions, and does not fully cover the substrate, it only occupies a negligible percentage of the total area, and therefore does not affect the TCE transparency. Remarkably, the best 20 mg/cm^3 s-MoO_x-treated AgNW TCE, which was annealed in N_2 atmosphere, has a transparency of ~96% in the whole wavelength range between 400 and 1000 nm. The optical transmittance and sheet resistance can be expressed by:

$$T(\lambda) = (1 + \frac{188.5}{R_S}\frac{\sigma_{OP}(\lambda)}{\sigma_{DC}})^{-2} \quad (1)$$

Where $\sigma_{OP}(\lambda)$ is the optical conductivity and σ_{DC} is the DC conductivity of the film. The TCE can be rated by a figure of merit (FoM), the ratio of $\sigma_{OP}(\lambda)/\sigma_{DC}$. The high and broad transmission spectrum with excellent low R_{sheet} in this sample corresponds to a very high FoM of 385.8.[23] This value is among the highest reported values in TCEs,[16, 47-49] indicating that s-MoO_x-treated AgNWs provide a promising alternative for ITO, which normally shows a FoM value of ~ 240.[16] Total reflection and film absorption (= 1 − R − T) spectra were also investigated. The results indicate that a further increase of MoO_x precursor concentration (80 and 160 mg/cm^3) not only results in a slightly lower conductivity, but also a significant increase in the reflectance (for 80 and 160 mg/cm samples) and absorption (160 mg/cm^3 sample). We attribute the inferior performance of higher

MoO_x precursor concentration samples to the formation of distinct pellet-shaped MoO_x aggregates that diffract light back to substrate and thus decrease the total transmission (**Figure 2 (e)**). The higher amount of MoO_x accumulating on the surface also contributes to the higher absorption of the sample. In the e-MoO_x-treated samples, the high absorption observed is due to the full coverage of MoO_x on the substrate surface. Higher reflection in the 30 nm e-MoO_x sample is caused by an interference effect of the high refractive index MoO_x ($n \approx 2$) on the low refractive index glass substrate ($n \approx 1.5$). In addition to total transmission and conductivity, the haze value also plays a critical role in the quality of TCEs, especially in see-through applications such as displays, touch panels, and windows. The haze value is defined as

$$Haze\ value = \frac{Forward\ scattered\ light}{Forward\ nonscattered\ light + Forward\ scattered\ light} \times 100\% \quad (2)$$

The haze value represents the degree of diffuse light scattering through a TCE. A high haze value corresponds to increased scattering and image blur, and is a common issue in nanowire-based TCEs because of the random distribution of nano/microstructures and the resultant rough surface, particularly in TCEs with densely packed nanowires.[17, 50-53] The total diffuse transmission and haze value of TCEs prepared with various treatments were studied, and the results are shown in **Figure 4 (d)** and **Table 1**. A low haze value of 0.57% is found in the TCE of pristine AgNWs. The 5 and 20 mg/mL s-MoO_x-treated samples have haze values of 0.87% and 0.90%, respectively. All three of these samples have haze values that are lower than the haze value normally required for various critical applications (1%).[54] Such a low haze value results from the low density of AgNWs used in this study (see **Figure 2**). A low-density AgNW matrix usually exhibits high R_{sheet}, such as in the case of the pristine AgNW TCE shown here (R_{sheet} = 4411 ohm/sq, **Table 1**). However, the s-MoO_x-treated samples show that with effective linking of nanowire junctions, excellent low resistance of less than 30 ohm/sq and a low haze value of 0.90% is still feasible in a AgNW-based TCE. Among all samples, the one treated with the 160 mg/mL s-MoO_x precursor displays the highest haze value, 3.17%, which is attributed to a large amount of aggregation and crystallization (see **Figure 2 (e)**) of the s-MoO_x on AgNWs, which causes a higher scattering effect. The transmission, reflection, absorption and haze data of the pure MoO_x films without AgNWs are listed in supporting information for reference.

While ITO-coated flexible substrates can be used in flexible applications, the brittle nature of ITO means that a strain of 1% or higher can cause the formation of irreversible cracks in the film.[55] As a consequence, AgNW networks coated on flexible plastic substrates have been intensively investigated as an alternative in flexible devices. The low glass transition temperature (T_g) of plastic substrates (ex: polyethylene naphthalate (PEN) $T_g \approx 120$ °C) restricts the nanowire linking approaches to relatively low temperatures. Heating the plastic substrate to a temperature equal to or greater than its T_g can cause its surface to wrinkle, especially when the surface area is large.[56] Therefore, nanowire fusing methods that require annealing temperatures greater than 120 °C may not be practical with flexible substrates.[57-59] The process of forming s-MoO_x on AgNWs in this study only requires a temperature of 100 °C, which makes it attractive for flexible substrates. To demonstrate the feasibility of our method, a large area (5 cm × 10 cm) s-MoO_x-treated AgNWs composite electrode on a PEN substrate was fabricated (**Figure 5 (a)**). The flexibilities of the best s-MoO_x-treated AgNW TCE (20 mg/mL precursor concentration, annealed in N_2 atmosphere) and ITO on PEN substrates were tested by subjecting the samples to a bending test. The instrument setup and the results are shown in **Figures 5 (b)** and **(c)**. Mechanical flexibility was evaluated by repeated tensile bending of the samples to a radius of 3 mm. The R_{sheet} of the s-MoO_x-treated AgNW TCE only increased from ~ 30 ohm/sq to 43 ohm/sq after 3000 bending cycles, which indicates good flexibility. In contrast, the R_{sheet} of ITO dramatically increased from 13.2 ohm/sq to 1.4 × 10^4 ohm/sq after only 700 bending cycles, which indicates very poor flexibility.

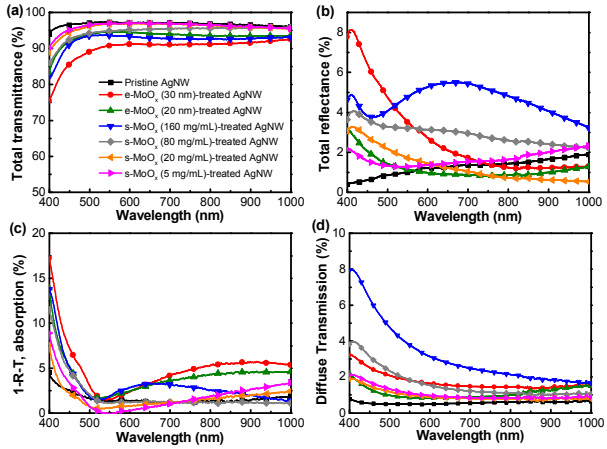

Figure 4. (a) Total transmittance (T), (b) total reflectance (R), (c) absorption (1 − R − T) and (d) diffuse transmission of AgNW TCEs. The s-MoO_x-treated AgNW TCEs were annealed in N_2 atmosphere.

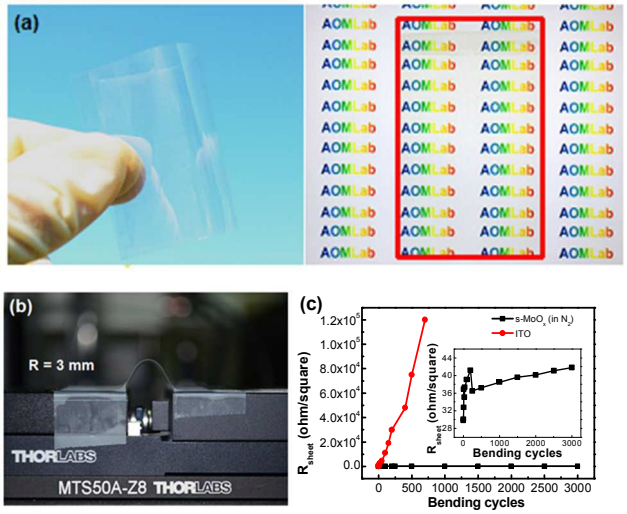

Figure 5. (a) Photograph of a large-area (5 cm × 10 cm) flexible TCE fabricated by s-MoO_x-treated AgNWs on PEN. (b) Photograph of a flexible TCE with a bending radius of 3 mm. (c) The resistance of s-MoO_x-treated AgNWs TCE and ITO during repeated bending testing (radius: 3 mm).

Table 1. Parameters of AgNW electrodes for various preparation methods.

AgNWs TCE	R_{sheet} (ohm/square)	Average total transmittance (%), [@ 550 nm]	Average total reflectance (%)	Average absorption (1 − R − T, %)	Haze value (%)

Pristine AgNW	4411	96.7, [97.3]	1.27	2.03	0.57
e-MoO_x (30 nm)-treated AgNW	3125	90.1, [90.8]	2.69	7.21	1.72
e-MoO_x (20 nm)-treated AgNW	2845	93.4, [94.6]	1.78	4.82	1.31
s-MoO_x (160 mg/mL)-treated AgNW	47.7	92.4, [93.6]	4.59	3.01	3.17
s-MoO_x (80 mg/mL)-treated AgNW	38.3	94.7, [94.9]	2.52	2.78	1.61
s-MoO_x (20 mg/mL)-treated AgNW	29.8	95.9, [96.8]	1.52	2.58	0.90
s-MoO_x (5 mg/mL)-treated AgNW	47.3	96.2, [96.9]	1.46	2.34	0.87

Average total reflectance values are taken over the wavelength range from 400 to 1000 nm. The s-MoO_x-treated AgNW TCEs were annealed in N_2 atmosphere.

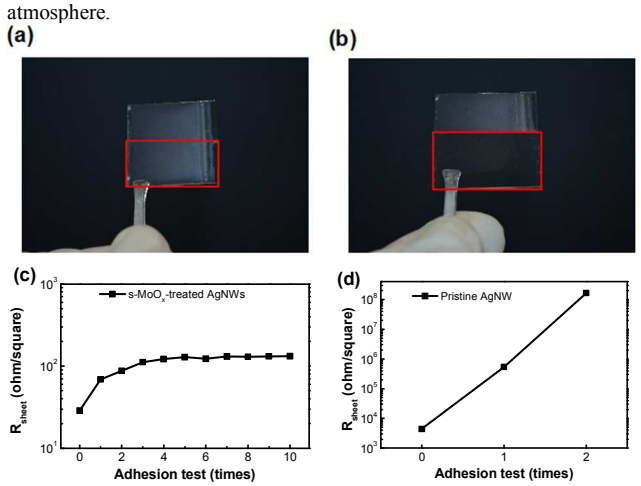

Figure 6. (a) s-MoO_x-treated AgNW TCE and (b) pristine AgNW TCE after the adhesion test. The rectangles indicate the area where the peeling tests were applied; variation of the R_{sheet} of (c) s-MoO_x-treated AgNW TCE and (d) pristine AgNW TCE as a function of the number of peeling cycles.

The s-MoO_x-treated AgNW TCE was also subjected to an adhesion test using 3M Scotch tape.[26] **Figures 6 (a)** and **(b)** show the s-MoO_x-treated and pristine AgNW TCEs after peeling the film repeatedly with the tape. The results show that the pristine AgNW TCE can be easily peeled off and thus has poor mechanical adhesion to the substrate. As shown in **Figure 6 (d)**, the R_{sheet} of this film increased dramatically with double peeling procedures (from 4411 ohm/sq to 1.2×10^8 ohm/sq). In contrast, the s-MoO_x treatment largely improved the adhesion of AgNWs on the substrate, and the film appearance remained uniform after the peeling test (**Figure 6 (a)**). As shown in **Figure 6 (c)**, only a slight increase of R_{sheet} was observed after the adhesion test (from ~ 30 ohm/sq to 132 ohm/sq). Therefore, s-MoO_x not only largely enhances the conductivity of AgNW films, but also effectively adheres the AgNWs to the substrate.

The structural and elemental compositions of the MoO_x-treated AgNW TCEs and pure MoO_x layers were analyzed with XPS and the results are shown in the supporting information. The XPS analysis investigated the oxidation states of the Mo atoms, and the Mo 3d spectra were carefully fitted with contribution from Mo^{6+}, Mo^{5+}, and Mo^{4+} oxidation states at 232.7, 231.2, and 229.5 eV, respectively.[60, 61] The XPS spectrum of s-MoO_x films annealed in an oxygen-rich environment (in air) shows that the Mo atoms are mainly in the Mo^{6+} oxidation state. In contrast, the MoO_x films prepared in the oxygen-deficient environment (e-MoO_x and s-MoO_x annealed in N_2) contain atoms in Mo^{6+}, Mo^{5+}, and Mo^{4+} oxidation states. This difference can be attributed to the formation of defect states arising from oxygen vacancies, which is in good agreement with the recent literature.[45, 62]

The work functions of the MoO_x-treated AgNW TCEs were measured by UPS. As shown in the supporting information, we find that all samples show high work functions of 5 ~ 5.4 eV. Slight lower work functions observed in s-MoO_x-treated AgNW samples can be attributed to the partly coverage of MoO_x on AgNWs. On closer inspection of the UPS spectra, it is found that both e-MoO_x and s-MoO_x TCEs annealed in N_2 display emissions from gap states in the range of 0.8–1.7 eV below the Fermi level, which is caused by the O-vacancies.[45, 61] No such trace can be found in the air-environment-annealed s-MoO_x sample. These results are consistent with the Mo compositions found in XPS measurements. The high work function and the existence of the gap state are believed to provide an efficient hole injection. Despite the fact that the e-MoO_x also shows the signal of these gap states in XPS and UPS results, the resistance performance in e-MoO_x-treated TCEs is still dominated by the poor contact between AgNWs at the intersections.

To demonstrate that the s-MoO_x-treated AgNW TCEs can readily be utilized in the optoelectronic applications, four TCEs were used to fabricate the ITO-free OLEDs: **(A)** pristine AgNW, **(B)** e-MoO_x-treated AgNW (20 nm), **(C)** s-MoO_x-treated AgNW (20mg/mL, annealed in N_2) and **(D)** s-MoO_x-treated AgNW (20 mg/mL, annealed in air). **Figure 7** shows a schematic of the OLED configuration and relative energy levels of the components. Noted that the gap states of the MoO_x exist only in **Device (B)** and **(C)**. **Figures 8 (a)** and **(b)** show the current density-voltage-luminance (*J*-V-L) characteristics of the devices. Low current density and luminance are found in Devices **(A)** and **(B)**, indicating retarded carrier transportation arising from poor TCEs. Because s-MoO_x achieves effective connection of the AgNWs as indicated by low R_{sheet}, devices **(C)** and **(D)** show much better electroluminance performance. Moreover, the gap state provides an improved hole injection efficiency from Ag to HAT-CN, which explains why the turn on voltage decreases from 3.3 V (annealed in air) to 2.9 V (annealed in N_2). **Device (C)** with annealed in N_2 s-MoO_x-treated AgNW TCE shows a low turn-on voltage of 2.9 V, a maximum power efficacy of 29.2 lm/W, and a maximum external quantum efficiency (E.Q.E.) of 10.3%. At high luminance, the **Device (C)**

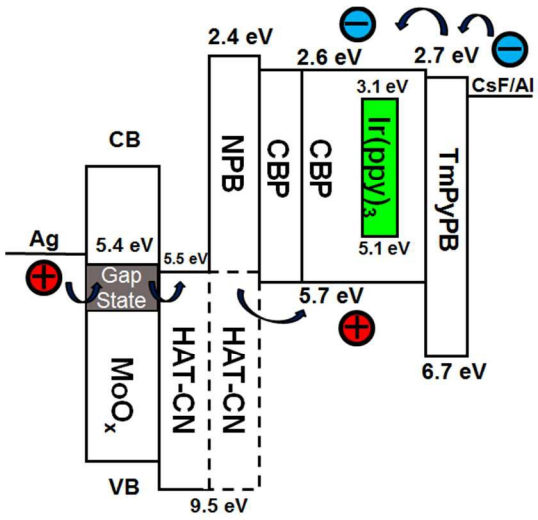

Figure 7. Energy band diagram of OLED device: Silver nanowire / MoO_x (four preparation methods: **(A)** pristine AgNW, **(B)** e-MoO_x-treated AgNW (20 nm), **(C)** s-MoO_x-treated AgNW (20mg/mL, annealed in N_2) and **(D)** s-MoO_x-treated AgNW (20 mg/mL, annealed in air)) / HAT-CN (10 nm) / NPB:HAT-CN (1.5%, 185 nm) / CBP (5 nm) / CBP:Ir(ppy)$_3$

(8%, 20 nm) / TmPyPB (20 nm) / CsF (1 nm) / Al.

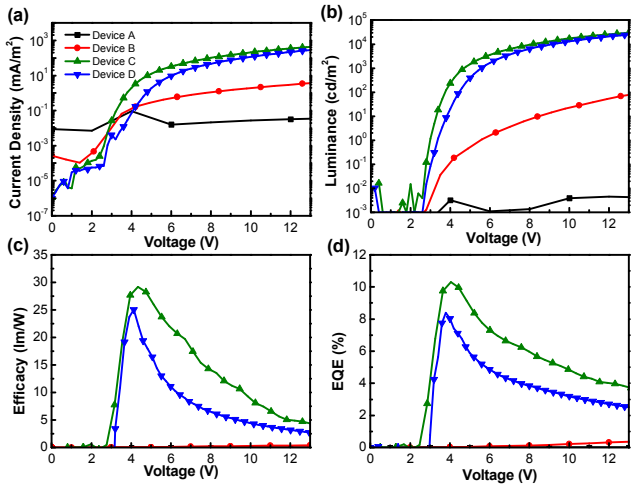

Figure 8. (a) Current density-voltage characteristics, (b) luminance-voltage characteristics, (c) power efficacy-luminance characteristics and (d) external quantum efficiency-luminance characteristics of AgNW-based, ITO-free OLEDs.

still maintained 28.2 lm/W and 10.2% E.Q.E. at 100 nits and 14.2 lm/W and 8.1% E.Q.E. at 1000 nits, respectively. The excellent performance of **Device (C)** can be attributed to a combination of characteristics of the N_2-enviroment-annealed, s-MoO_x-treated AgNW TCE, which include low R_{sheet}, high carrier conductivity, and good hole injection capability. The ITO-based OLEDs with same device structure were fabricated and their characteristics are shown in **Figure S8** in the supporting information. The AgNW electrode devices achieve ~ 90% E.Q.E. of which the ITO electrode device counterparts can obtain. Slight lower efficiency in AgNW TCE devices is attributed to the higher surface roughness of AgNW TCEs and thus the higher leakage current in AgNW-based devices.

Table 2. Performance of AgNW-based OLEDs with various preparation methods.

AgNW TCEs	Turn on voltage (0.1 cd/m²)	Power efficacy (lm/W)	External quantum efficiency (%)
		@ max, 100 cd/m², 1000 cd/m²	
Pristine AgNW	-	-, -, -	-, -, -
e-MoO_x(20 nm)-treated AgNW	5.4 V	0.4, 0.1, 0.1	0.3, 0.1, 0.2
s-MoO_x(Annealed in N_2)-treated AgNW	2.9V	29.2, 28.2, 14.2	10.3, 10.2, 8.1
s-MoO_x(Annealed in air)-treated AgNW	3.3 V	25.1, 17.9, 10.2	8.3, 7.1, 5.2

Conclusions

In summary, we have demonstrated the fabrication of s-MoO_x-treated AgNW TCEs utilizing low-temperature (sub-100 °C) processes. The solution-processed s-MoO_x-treated AgNW TCEs exhibit a combination of several promising characteristics, such as high and broad transmittance across a wavelength range of 400 to 1000 nm, total transmission of up to 95.9%, low R_{sheet} of 29.8 ohm/sq, low haze value of 0.90%, better adhesion on the substrate, good flexibility, and preferable gap states for efficient hole injection in optoelectronic applications. By utilizing the s-MoO_x-treated AgNW TCE as the anode in ITO-free OLEDs, promising performance results of 29.2 lm/W and 10.3% E.Q.E. are demonstrated. The versatile, multi-functional s-MoO_x treatment presented here paves the way for the use of low-temperature, solution-processed MoO_x as both a nanowire conductivity enhancer and a hole injection interfacial layer for future flexible optoelectronic devices.

Acknowledgements

The authors would like to acknowledge financial support from the Ministry of Science and Technology of Taiwan (102-2221-E-007-125-MY3, 101-2112-M-007-017-MY3, 102-2633-M-007-002, 103-3113-E-007-004), and the Low Carbon Energy Research Center, National Tsing Hua University. SEM images were taken in the Center for Nanotechnology, Materials Science, Microsystems (CNMM) of the National Tsing Hua University, which is partly supported by the Ministry of Science and Technology of Taiwan.

Notes and references

1. J. Ouyang, Q. Xu, C.-W. Chu, Y. Yang, G. Li and J. Shinar, *Polymer*, 2004, **45**, 8443-8450.
2. Y. Xia and J. Ouyang, *Macromolecules*, 2009, **42**, 4141-4147.
3. U. Lang, E. Müller, N. Naujoks and J. Dual, *Adv. Funct. Mater.*, 2009, **19**, 1215-1220.
4. Y. Zhu and F. Xu, *Adv. Mater.*, 2012, **24**, 1073-1077.
5. M. K. Shin, J. Oh, M. Lima, M. E. Kozlov, S. J. Kim and R. H. Baughman, *Adv. Mater.*, 2010, **22**, 2663-2667.
6. K. Liu, Y. Sun, P. Liu, X. Lin, S. Fan and K. Jiang, *Adv. Funct. Mater.*, 2011, **21**, 2721-2728.
7. B. Y. Ahn, D. J. Lorang and J. A. Lewis, *Nanoscale*, 2011, **3**, 2700-2702.
8. T.-H. Han, Y. Lee, M.-R. Choi, S.-H. Woo, S.-H. Bae, B. H. Hong, J.-H. Ahn and T.-W. Lee, *Nature Photon.*, 2012, **6**, 105-110.
9. S. Bae, H. Kim, Y. Lee, X. Xu, J. S. Park, Y. Zheng, J. Balakrishnan, T. Lei, H. R. Kim, Y. I. Song, Y. J. Kim, K. S. Kim, B. Ozyilmaz, J. H. Ahn, B. H. Hong and S. Iijima, *Nature nanotechnology*, 2010, **5**, 574-578.
10. R. H. Kim, M. H. Bae, D. G. Kim, H. Cheng, B. H. Kim, D. H. Kim, M. Li, J. Wu, F. Du, H. S. Kim, S. Kim, D. Estrada, S. W. Hong, Y. Huang, E. Pop and J. A. Rogers, *Nano Lett.*, 2011, **11**, 3881-3886.
11. J. Liang, L. Li, K. Tong, Z. Ren, W. Hu, X. Niu, Y. Chen and Q. Pei, *ACS Nano*, 2014, **8**, 1590-1600.
12. Y.-J. Noh, S.-S. Kim, T.-W. Kim and S.-I. Na, *Sol. Energy Mater. Sol. Cells*, 2014, **120**, 226-230.
13. D. P. Langley, G. Giusti, M. Lagrange, R. Collins, C. Jiménez, Y. Bréchet and D. Bellet, *Sol. Energy Mater. Sol. Cells*, 2014, **125**, 318-324.
14. L. Li, J. Liang, S. Y. Chou, X. Zhu, X. Niu, ZhibinYu and Q. Pei, *Scientific reports*, 2014, **4**, 4307.
15. H. G. Im, J. Jin, J. H. Ko, J. Lee, J. Y. Lee and B. S. Bae, *Nanoscale*, 2014, **6**, 711-715.
16. D. Y. Choi, H. W. Kang, H. J. Sung and S. S. Kim, *Nanoscale*, 2013, **5**, 977-983.

17. C. Preston, Z. Fang, J. Murray, H. Zhu, J. Dai, J. N. Munday and L. Hu, *Journal of Materials Chemistry C*, 2014, **2**, 1248.
18. X. Zhang, X. Yan, J. Chen and J. Zhao, *Carbon*, 2014, **69**, 437-443.
19. Jiajie Liang, Lu Li, Kwing Tong, Zhi Ren, Wei Hu, Xiaofan Niu, Yongsheng Chen and Q. Pei, in *ACS Nano*, 2014, vol. 8, pp. 1590-1600.
20. T. B. Song, Y. Chen, C. H. Chung, Y. M. Yang, B. Bob, H. S. Duan, G. Li, K. N. Tu, Y. Huang and Y. Yang, *ACS Nano*, 2014, **8**, 2804-2811.
21. S. Nam, H. W. Cho, S. Lim, D. Kim, H. Kim and B. J. Sung, *ACS Nano*, 2013, **7**, 851-856.
22. H. Wu, D. Kong, Z. Ruan, P. C. Hsu, S. Wang, Z. Yu, T. J. Carney, L. Hu, S. Fan and Y. Cui, *Nature nanotechnology*, 2013, **8**, 421-425.
23. S. De, T. M. Higgins, P. E. Lyons, E. M. Doherty, P. N. Nirmalraj, W. J. Blau, J. J. Boland and J. N. Coleman, *ACS Nano*, 2009, **3**, 1767-1774.
24. M. S. Lee, K. Lee, S. Y. Kim, H. Lee, J. Park, K. H. Choi, H. K. Kim, D. G. Kim, D. Y. Lee, S. Nam and J. U. Park, *Nano Lett.*, 2013, **13**, 2814-2821.
25. J. Lee, P. Lee, H. B. Lee, S. Hong, I. Lee, J. Yeo, S. S. Lee, T.-S. Kim, D. Lee and S. H. Ko, *Adv. Funct. Mater.*, 2013, **23**, 4171-4176.
26. L. Hu, H. S. Kim, J. Y. Lee, P. Peumans and Y. Cui, *ACS Nano*, 2010, **4**, 2955-2963.
27. K. Zilberberg, F. Gasse, R. Pagui, A. Polywka, A. Behrendt, S. Trost, R. Heiderhoff, P. Görrn and T. Riedl, *Adv. Funct. Mater.*, 2014, **24**, 1671-1678.
28. R. Zhu, C. H. Chung, K. C. Cha, W. Yang, Y. B. Zheng, H. Zhou, T. B. Song, C. C. Chen, P. S. Weiss, G. Li and Y. Yang, *ACS Nano*, 2011, **5**, 9877-9882.
29. E. C. Garnett, W. Cai, J. J. Cha, F. Mahmood, S. T. Connor, M. Greyson Christoforo, Y. Cui, M. D. McGehee and M. L. Brongersma, *Nat. Mater.*, 2012, **11**, 241-249.
30. J. Jiu, M. Nogi, T. Sugahara, T. Tokuno, T. Araki, N. Komoda, K. Suganuma, H. Uchida and K. Shinozaki, *J. Mater. Chem.*, 2012, **22**, 23561.
31. F. Liu, S. Shao, X. Guo, Y. Zhao and Z. Xie, *Sol. Energy Mater. Sol. Cells*, 2010, **94**, 842-845.
32. W. J. Dong, G. H. Jung and J.-L. Lee, *Sol. Energy Mater. Sol. Cells*, 2013, **116**, 94-101.
33. L. Chen, P. Wang, F. Li, S. Yu and Y. Chen, *Sol. Energy Mater. Sol. Cells*, 2012, **102**, 66-70.
34. M.-F. Xu, L.-S. Cui, X.-Z. Zhu, C.-H. Gao, X.-B. Shi, Z.-M. Jin, Z.-K. Wang and L.-S. Liao, *Org. Electron.*, 2013, **14**, 657-664.
35. S. Höfle, H. Do, E. Mankel, M. Pfaff, Z. Zhang, D. Bahro, T. Mayer, W. Jaegermann, D. Gerthsen, C. Feldmann, U. Lemmer and A. Colsmann, *Org. Electron.*, 2013, **14**, 1820-1824.
36. Y. Sun, J. H. Seo, C. J. Takacs, J. Seifter and A. J. Heeger, *Adv. Mater.*, 2011, **23**, 1679-1683.
37. H. J. Bolink, E. Coronado, J. Orozco and M. Sessolo, *Adv. Mater.*, 2009, **21**, 79-82.
38. T. Matsushima, G.-H. Jin, Y. Kanai, T. Yokota, S. Kitada, T. Kishi and H. Murata, *Org. Electron.*, 2011, **12**, 520-528.
39. J. Meyer, R. Khalandovsky, P. Gorrn and A. Kahn, *Adv. Mater.*, 2011, **23**, 70-73.
40. A. Buckley, D. Pickup, C. Yates, Y. Zhao and D. Lidzey, *J. Appl. Phys.*, 2011, **109**, 084509.
41. M. Kröger, S. Hamwi, J. Meyer, T. Riedl, W. Kowalsky and A. Kahn, *Appl. Phys. Lett.*, 2009, **95**, 123301.
42. M. D. Earle, *Phys Rev*, 1942, **61**, 56-63.
43. N. Miyayta, T. Suzuki and R. Ohyamy, *Thin Solid Films*, 1996, 218-222.
44. J.-H. Chang, H.-F. Wang, W.-C. Lin, K.-M. Chiang, K.-C. Chen, W.-C. Huang, Z.-Y. Huang, H.-F. Meng, R.-M. Ho and H.-W. Lin, *J. of Mater. Chemistry*, 2014, **2**, 13398.
45. P.-S. Wang, Y.-Y. Lo, W.-H. Tseng, M.-H. Chen and C.-I. Wu, *J. Appl. Phys.*, 2013, **114**, 063710.
46. P.-S. Wang, I. W. Wu, W.-H. Tseng, M.-H. Chen and C.-I. Wu, *Appl. Phys. Lett.*, 2011, **98**, 173302.
47. Y. Jin, D. Deng, Y. Cheng, L. Kong and F. Xiao, *Nanoscale*, 2014, **6**, 4812-4818.
48. J. H. Yim, S. Y. Joe, C. Pang, K. M. Lee, H. Jeong, J. Y. Park, Y. H. Ahn, J. C. de Mello and S. Lee, *ACS Nano*, 2014, **8**, 2857-2863.
49. A. Kim, Y. Won, K. Woo, C. H. Kim and J. Moon, *ACS Nano*, 2013, **7**, 1081-1091.
50. C. Preston, Y. Xu, X. Han, J. N. Munday and L. Hu, *Nano Res*, 2013, **6**, 461-468.
51. A. B. V. Kiran Kumar, C. wan Bae, L. Piao and S.-H. Kim, *Mater. Res. Bull.*, 2013, **48**, 2944-2949.
52. S. Mehra, M. G. Christoforo, P. Peumans and A. Salleo, *Nanoscale*, 2013, **5**, 4400-4403.
53. T. Araki, J. Jiu, M. Nogi, H. Koga, S. Nagao, T. Sugahara and K. Suganuma, *Nano Res*, 2014, **7**, 236-245.
54. D. S. and R. B. Kaner, *Materials Research Society*, 2011, **36**, 749-755.
55. Z. Yu, Q. Zhang, L. Li, Q. Chen, X. Niu, J. Liu and Q. Pei, *Adv. Mater.*, 2011, **23**, 664-668.
56. D. G. Howells, B. M. Henry, J. Madocks and H. E. Assender, *Thin Solid Films*, 2008, **516**, 3081-3088.
57. J. Lee, I. Lee, T. S. Kim and J. Y. Lee, *Small*, 2013, **9**, 2887-2894.
58. H. H. Khaligh and I. A. Goldthorpe, *Nano Research Letters*, 2013, **8**, 235-241.
59. T. Tokuno, M. Nogi, M. Karakawa, J. Jiu, T. T. Nge, Y. Aso and K. Suganuma, *Nano Res*, 2011, **4**, 1215-1222.
60. M. Vasilopoulou, A. M. Douvas, D. G. Georgiadou, L. C. Palilis, S. Kennou, L. Sygellou, A. Soultati, I. Kostis, G. Papadimitropoulos, D. Davazoglou and P. Argitis, *J. Am. Chem. Soc.*, 2012, **134**, 16178-16187.
61. K. H. Wong, K. Ananthanarayanan, J. Luther and P. Balaya, *J. Phys. Chem. C*, 2012, **116**, 16346-16351.
62. B. Dasgupta, W. P. Goh, Z. E. Ooi, L. M. Wong, C. Y. Jiang, Y. Ren, E. S. Tok, J. Pan, J. Zhang and S. Y. Chiam, *J. Phys. Chem. C*, 2013, **117**, 9206-9211.